EFFECTS OF BUBBLE LOCATION ON PORE SHAPE IN SOLID

S. Y. Hsiao **P. S. Wei***

Department of Mechanical and Electro-Mechanical Engineering
National Sun Yat-Sen University
Kaohsiung, Taiwan

ABSTRACT

The shapes of a pore resulting from an entrapped bubble by a solidification front for different locations of the bubble below the free surface are predicted in this work. Bubble location is an important factor affecting temperature gradient in liquid, solute gas dissipated into the ambient, heterogeneous nucleation of the bubble and shape of the bubble cap, and subsequent entrapment and the pore shape in solid. The shapes of pores in solid influence not only material properties, but also contemporary issues of engineering, biology, medical technology and science, etc. This study takes into account solute transport across a coupling shape of the pore cap determined by the Young-Laplace equation governing balance of liquid, gas and capillary pressures. The results find that increases in depthwise location of a bubble increase pore radius and time for bubble entrapment as solute transport is from the pore across cap emerged through a concentration boundary layer along the solidification front into surrounding liquid in the early stage. On the other hand, the bubble cannot be entrapped, provided that solute transport in opposite directions across the cap submerged in a concentration boundary layer along the solidification front. The predicted growth and entrapment of a tiny bubble as a pore in solid agree with experimental data. Understanding and controlling of the pore shape via controlling bubble location is of interest and challenging.

Keywords: Pore formation, Bubble entrapment, Porosity, Porous material.

1. INTRODUCTION

Substances containing a number of pores have characteristics different from those of bulk substances, such as a low density and a large surface area. Therefore, they can be utilized as lightweight materials, catalysts, electrodes, vibration and acoustic energy absorption materials, impact energy absorption materials, and scaffold to tissue ingrowth, etc. [1, 2]. Porosity, however, degrades mechanical properties and impedes efficiency or functional properties of products [3-6]. Finding critical factors affecting and controlling pore formation is therefore challenging.

The location of the bubble below the free surface of liquid is an important factor affecting pore formation in solid. Solute gas can be easily dissipated to the atmosphere through the entire liquid layer in a thickness of less than 1 mm, which can be scaled as the ratio between solute diffusivity around 10^{-9} m^2/s and solidification rate around 10^{-6} m/s. Solute gas concentration in the pore is influenced by either solute gas concentration in the liquid ahead of the solidification or that away from the solidification front. Directions and magnitudes of mass transfer rate thus can be different. Liquid pressure enhances heterogeneous nucleation of a bubble on a solidification front [7]. Hydrostatic pressure, representing the product of thickness and density of liquid layer and gravitational acceleration, is nearly identical to liquid pressure, provided that fluid flow is small and the driving force is gravitational force. The free-energy barrier, nucleation rates, and corresponding critical radius of bubble formation are reduced by increasing liquid pressure around the bubble cap and thickness of the liquid layer. The critical velocity responsible for an entrapped bubble in solid decreases as liquid pressure increases [8, 9]. The bubble shape is also affected by liquid pressure to satisfy the Young-Laplace equation at the bubble cap. Tracing contact angle of the bubble cap during solidification delineates the pore shape in solid [10]. An increase in bubble location also decreases temperature gradient in the liquid and increases solidification rate. The latter enhances instability of the solidification front [3, 5, 11], sites for bubble nucleation [12, 13], bubble entrapment [14, 15], solute gas transport across the bubble cap [16, 17], and reduces porosity [12, 17, 18] and pore sizes [2, 12, 13, 17, 18] in solid.

In this work, the shape of a pore, resulting from a bubble entrapped by a solidification front, for different

* Corresponding author (pswei@mail.nsysu.edu.tw)

DOI : 10.1017/jmech.2017.90
Copyright © 2017 The Society of Theoretical and Applied Mechanics
https://doi.org/10.1017/jmech.2017.90 Published online by Cambridge University Press

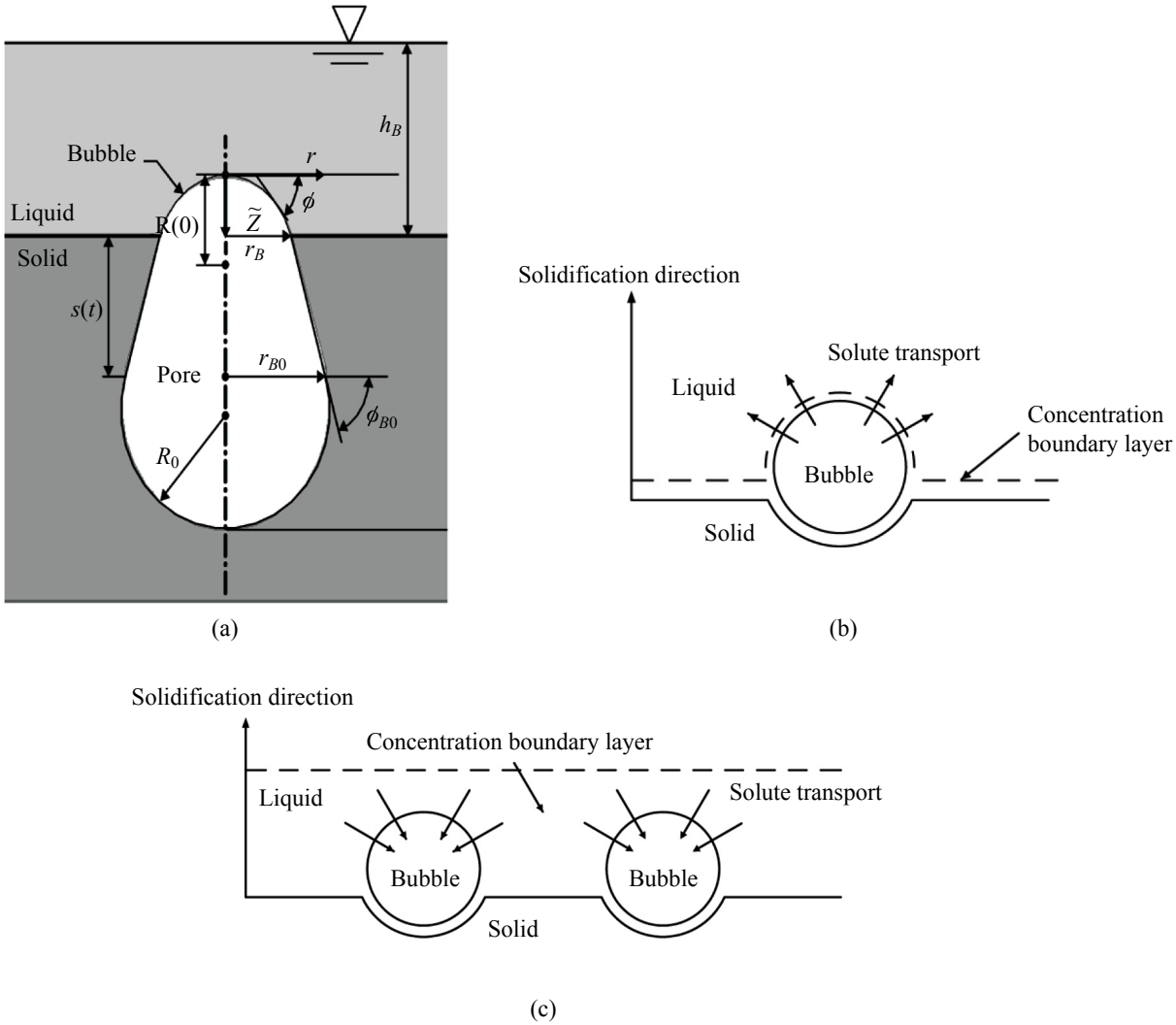


Fig. 1 Schematic sketch of (a) physical model, (b) the cap emerged through a thin concentration boundary layer along a solidification front in Case 1, and (c) the cap submerged into a thick concentration boundary layer in Case 2.

location of the bubble is predicted. Different directions and magnitudes of solute transport across the bubble cap are accounted. Controlling of the growth of the pore shape via bubble location is therefore obtained.

2. SYSTEM MODEL AND ANALYSIS

A pore resulting from entrapment of a bubble by a solidification front is illustrated in Fig. 1(a). The pore shape in solid to a first approximation can be delineated by tracing the contact angle of the bubble cap [10, 14, 15]. A realistic shape of the bubble cap beyond the solidification front is therefore required and determined by the Young-Laplace equation, governing normal stress balance between gas, capillary and liquid pressures. Solute gas pressure in the pore is determined by solute transport across the cap in different directions, as illustrated in Figs. 1(b) and (c). In the former, solute concentration in the pore is greater than that in surrounding liquid, since the bubble is nucleated due to supersaturation. Solute is therefore transferred from the pore across the cap emerged through the thin concentration boundary layer into surrounding liquid. In the latter, conservation of solute within the thick concentration boundary layer results in solute transport from surrounding liquid into the submerged cap during solidification. The location of the bubble is measured from the free surface of the liquid layer, which also stands for thickness of the liquid layer.

The major assumptions made are the following:

1. The model system is axisymmetric.
2. The tiny bubble characterized by a small Bond number leads to apply available perturbation solutions to predict a lumped micro-bubble shape in a nearly spherical cap. Bond number for a bubble cap in microscale is much less than unity.
3. Liquid is static. Liquid pressure is therefore hydrostatic pressure.
4. Unsteady solute concentration in the pore resulting from solute transport across the cap in Case 1 can be given by [16]

$$\frac{d\tilde{n}_g}{d\tilde{t}} = \tilde{h}_D \tilde{A}_c (\tilde{C}_\infty - \tilde{C}_c) \tag{1}$$

https://doi.org/10.1017/jmech.2017.90 Published online by Cambridge University Press

where $\tilde{h}_D$ is the mass transfer coefficient, $\tilde{n}_g$ is solute content in the pore, $\tilde{C}_\infty$ and $\tilde{C}_c$ are, respectively, solute concentration far from the solidification front and bubble cap. Since the bubble is heterogeneously nucleated due to super-saturation, higher solute concentration in the pore than that in liquid results in solute transport from the pore across cap into surrounding liquid in the early stage. On the other hand, solute transport in Case 2 is transferred from surrounding liquid into the pore, given by [10, 17, 18]

$$\frac{d\tilde{n}_g}{d\tilde{t}} = \tilde{h}_D \tilde{A}_c (\tilde{C}_c - \tilde{C}_\infty) \tag{2}$$

where the first term on the right-hand side of Eq. (2) can be considered as a solute source, because solute concentration in liquid is accumulated ahead of the solidification front.

5. Physico-chemical equilibrium or Henry's law is satisfied at the bubble cap

$$\tilde{C}_c = \frac{\tilde{p}_g}{\tilde{K}} \tag{3}$$

where K is Henry's law constant.

6. Pore shape is delineated by tracing contact angle of the bubble cap beyond the solidification front and given by

$$\frac{dr_B}{ds} = \frac{1}{\tan(\pi - \phi_B)} \tag{4}$$

With the above assumptions, the governing equation of solute gas pressure in the pore can be obtained by taking time derivative of the equation of state

$$\frac{d\tilde{p}_g}{d\tilde{t}}\tilde{V} + \tilde{p}_g \frac{d\tilde{V}}{d\tilde{t}} = \frac{d\tilde{n}_g}{d\tilde{t}} \tilde{R}_u \tilde{T} \tag{5}$$

Substituting Eqs. (1) and (3) into (5) leads to a dimensionless equation governing solute gas pressure in the pore in Case 1

$$\frac{dp_g}{dt} + \frac{p_g A_c}{V}\left(\frac{1}{A_c}\frac{dV}{dt} + \frac{h_D}{K}\right) = \frac{h_D Bo A_c}{V} C_\infty \tag{6}$$

where Bond number Bo indicates the ratio between hydrostatic pressure and capillary pressure in a length scale of initial bubble radius. Substituting Eqs. (2) and (3) into (5), dimensionless equation for solute gas pressure in the pore in Case 2 yields

$$\frac{dp_g}{dt} + \frac{p_g A_c}{V}\left(\frac{1}{A_c}\frac{dV}{dt} - \frac{h_D}{K}\right) = -\frac{h_D Bo A_c}{V} C_\infty \tag{7}$$

Examining Eqs. (6) and (7) reveals three cases

$$\frac{1}{A_c}\frac{dV}{dt} + \frac{h_D}{K} > 0 \quad \text{for Case 1} \tag{8}$$

$$\frac{1}{A_c}\frac{dV}{dt} - \frac{h_D}{K} < 0 \quad \text{for Case 2a} \tag{9}$$

$$\frac{1}{A_c}\frac{dV}{dt} - \frac{h_D}{K} > 0 \quad \text{for Case 2b} \tag{10}$$

which show there exist three cases to determine time-dependent solute gas pressure in the pore, depending on expansion or shrinkage of pore volume and different magnitude and directions of solute transport across the bubble cap. The total pore volume in Eqs. (6) or (7) is evaluated by

$$V = V_c + V_w \tag{11}$$

where volume of the bubble cap and volume below the solidification front yield, respectively,

$$V_c = \int_0^{\phi_B} \pi r^2 \frac{dz'}{d\phi} d\phi \tag{12}$$

$$V_w = V_{w0} + \int_0^t \pi r_B^2 \frac{ds}{dt'} dt' \tag{13}$$

Radius and contact angle of the bubble cap on the solidification front in Eq. (12) can be determined as long as the shape of the bubble cap is found. The cap shape in absence of an inflection point and neck region was found to be [19]

$$r = f(\phi, R(0), Bo) \tag{14}$$

$$z = g(\phi, R(0), Bo) \tag{15}$$

where apex radius of the cap is

$$R(0) = \frac{2}{2 + p_g - p_{g0} + Bo(h_{B0} - h_B - z_{B0} + z_B)} \tag{16}$$

Solution procedure is shown in the flow chart in Fig. 2. Computation starts by selecting initial conditions of bubble radius $R(0) = 1$, contact angle ϕ_{B0}, and thickness of the liquid layer beyond the solidification front h_{B0}, and independent parameters of solidification rate U, Henry's law constant K, initial solute concentration C_∞, *Bond number* Bo, and mass transfer coefficient h_D, etc. Cap base radius r_B is calculated from Eq. (4). Equations (14) and (15) are solved to determine contact angle ϕ_B, and cap height z_B, respectively. The total pore volume V is obtained by summing Eqs. (12) and (13) governing pore volume in the cap and pore below the solidification front, respectively. After solute gas pressure p_g in the pore is found from Eqs. (6) or (7), apex radius $R(0)$ is calculated from Eq. (16). Computation is repeated to the next time.

3. RESULTS AND DISCUSSION

This work studies the effects of bubble location on pore formation in three different mechanisms, as dis-

https://doi.org/10.1017/jmech.2017.90 Published online by Cambridge University Press

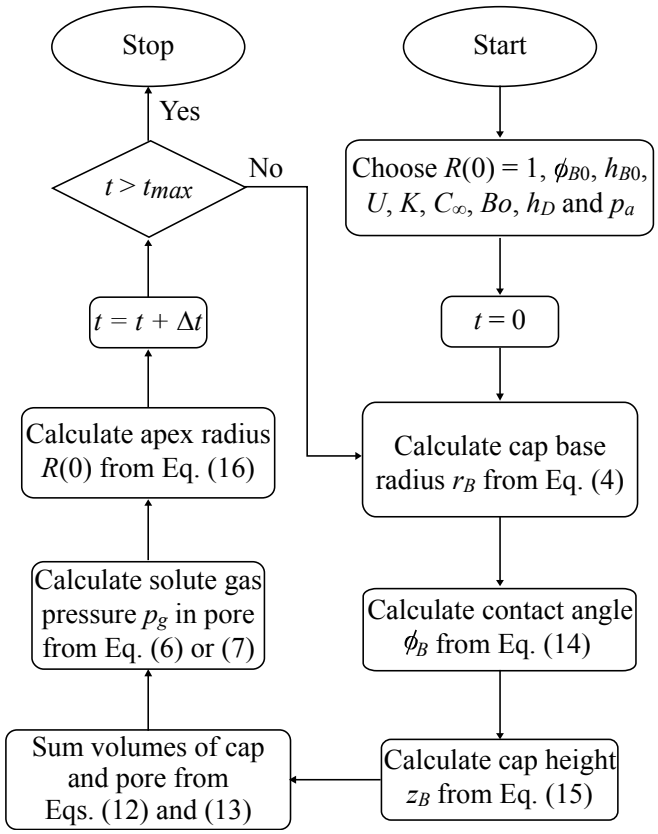


Fig. 2 Flow chart for solution procedure.

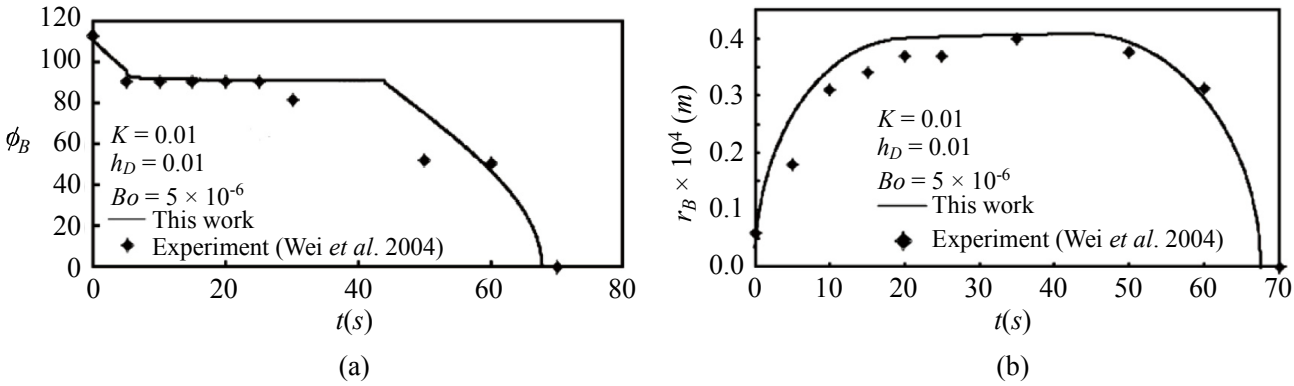


Fig. 3 Comparison between measured and predicted development of the pore shape as functions of time.

cussed previously. The bubble location reflects thickness of the liquid layer beyond the solidification front. Independent dimensionless parameters are estimated from a tiny bubble in a typical size of 10^{-4} – 10^{-6} m nucleated on a solidification front with a solidification rate 10^{-5} – 10^{-6} m/s in cooling water containing a dissolved carbon dioxide gas around 0.001-0.3 wt%, mass transfer coefficient of 10^{-6} m/s, Henry's law constant of 10^6 – 10^8 Pa/wt%.

Figures 3(a) and (b) show predicted contact angle and cap or pore radius as functions of time agree with measurements [20] in the solidification of water containing carbon dioxide of 0.351g/100g at a cold temperature of -25°C, respectively. There exists a long period of time at the contact angle around 90 degrees corresponding the maximum pore radius.

In Case 1, an increase in dimensionless bubble location increases radius and length of the pore, and time for bubble entrapment, as can be seen in Fig. 4(a). Figure 4(b) shows that an increase in dimensionless bobble location increases and slightly decreases solute concentration at the cap in the early and late stages, respectively. This is because solute gas pressure in the pore increases with bubble location, as can be seen from Eq. (17), resulting in an increase in solute concentration at the cap (see Eq. (3)) in the early stage

$$p_g = Bo(h_B - z_B) + p_a + \frac{2}{R(0)} \tag{17}$$

https://doi.org/10.1017/jmech.2017.90 Published online by Cambridge University Press

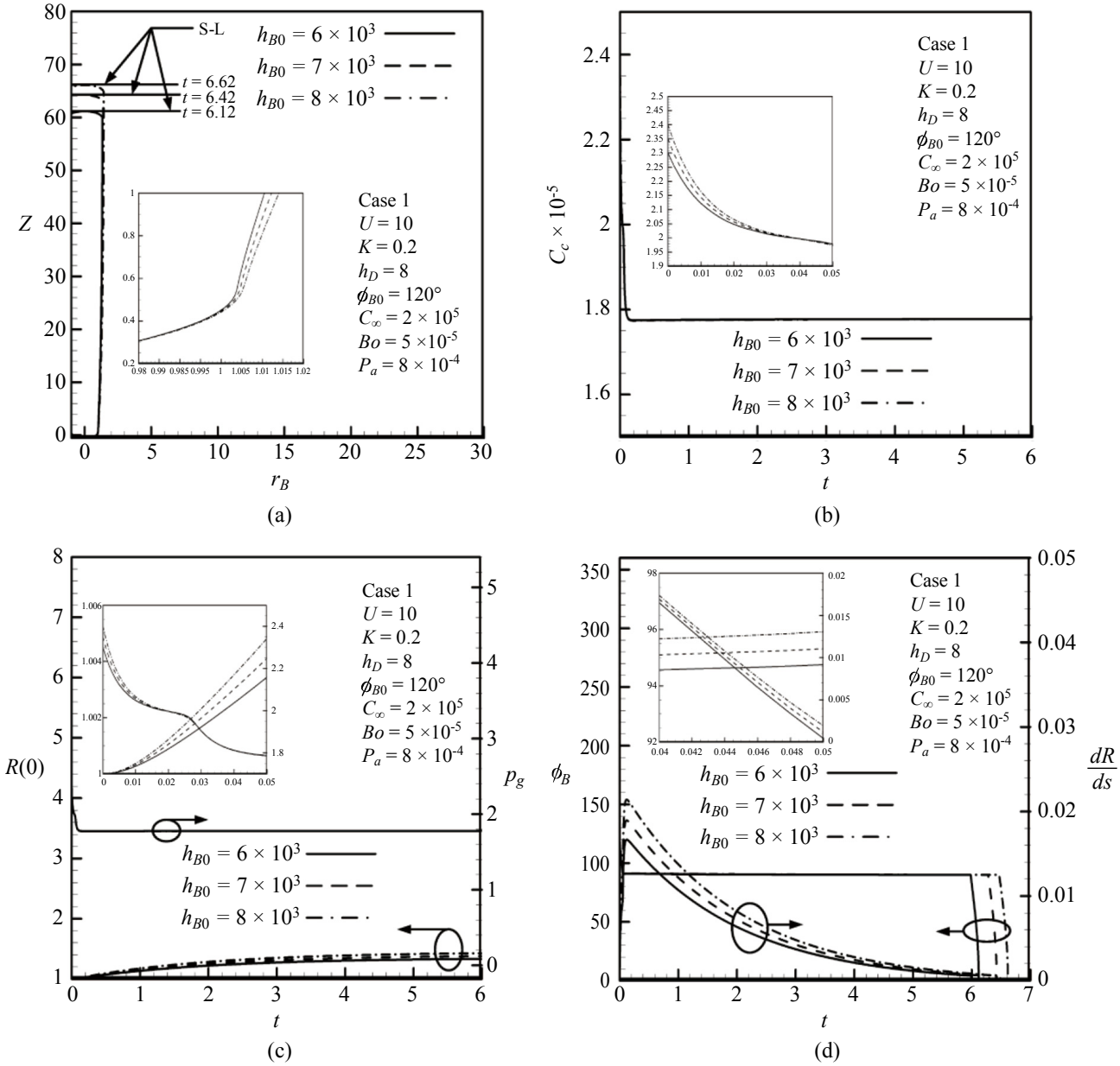


Fig. 4 Predicted (a) pore shape, and (b) dimensionless solute concentration at the cap, (c) dimensionless apex radius and solute gas pressure, and (d) contact angle and bubble growth rate-to-solidification rate ratio as functions of time for different dimensionless bubble locations in Case 1.

Dimensionless solute concentrations at the cap decreases more rapidly for a higher bubble location in the early stage. The rapid decrease in solute concentration at the cap results from both expansion rate of pore volume and solute transport from the pore into surrounding liquid. Relatively constant solute concentration at the cap in late stage, however, reflects a balance between expansion of pore volume and solute transfer from the surrounding liquid into pore. Figure 4(c) shows that the corresponding dimensionless solute gas pressure in the pore increases and decreases in the early and late stages, respectively, as dimensionless bubble location increases. This trend is similar to that of solute concentration at the cap (see Fig. 4(b)) in order to satisfy Henry's law (see Eq. (3)). Dimensionless apex radius increases with dimensionless bubble location in the course of solidification. It is noted that increased apex radius of the cap depends on the drop of solute gas pressure in the pore. In Fig. 4(d), an increase in bubble location reduces drop of contact angle in early stage. Contact angle then maintains a relative constant value near 90 degrees for a long period, which increases with bubble location. An increase in bubble location increases the bubble growth rate-to-solidification rate ratio and its peak, and delay time to become zero at which contact angle passes through 90 degrees, leading to entrapment of the bubble [14, 15].

In Case 2a, an increase in dimensionless bubble location increases pore radius, as shown in Fig. 5(a). However, the cap is not entrapped by the solidification front. In contrast to Fig. 4(b), Fig. 5(b) shows that solute concentration at the cap maintains relatively constant in the

https://doi.org/10.1017/jmech.2017.90 Published online by Cambridge University Press

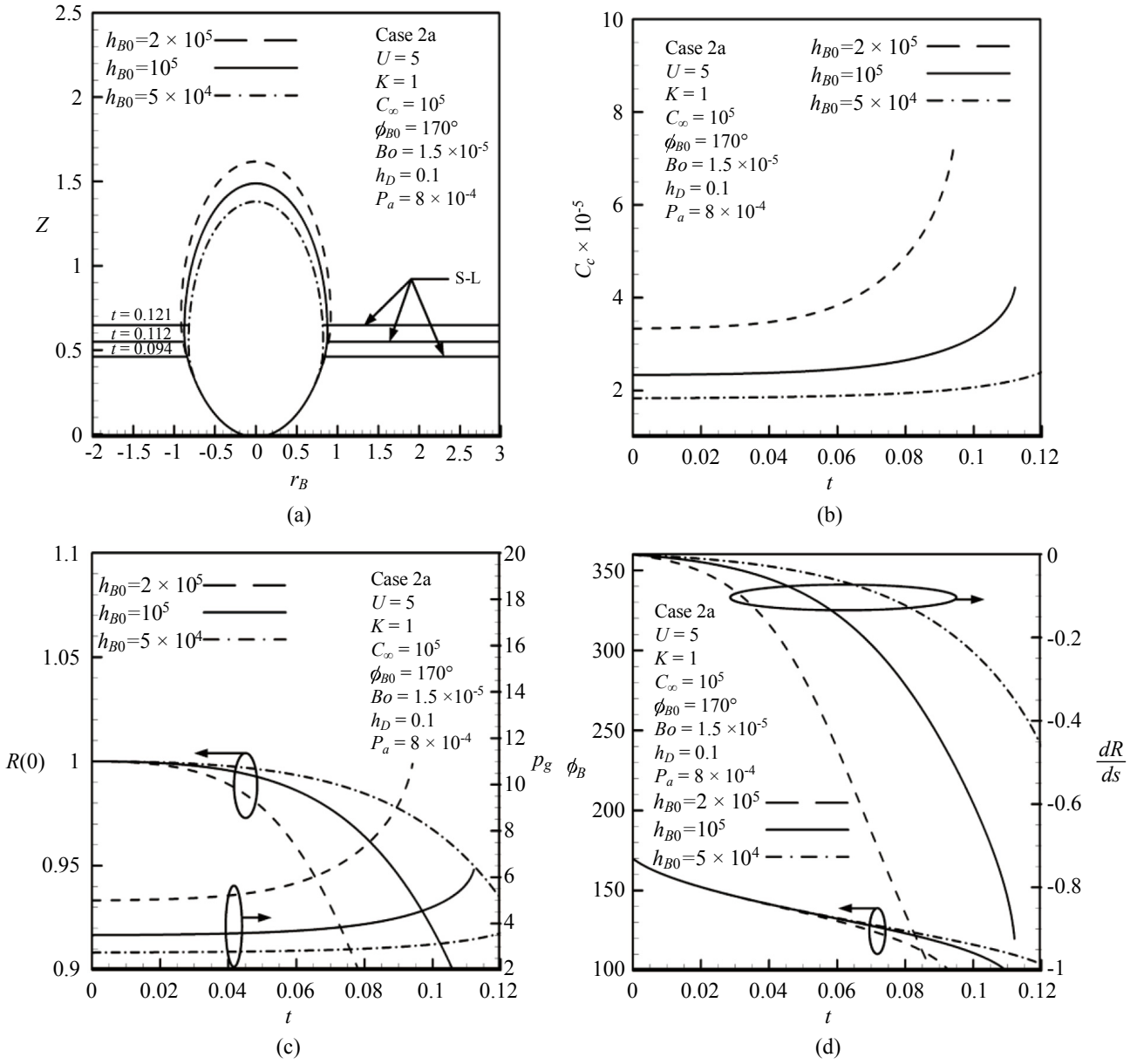


Fig. 5. Predicted (a) pore shape, and (b) dimensionless solute concentration at the cap, (c) dimensionless apex radius and solute gas pressure, and (d) contact angle and bubble growth rate-to-solidification rate ratio as functions of time for different dimensionless bubble locations in Case 2a.

early stage and increases significantly in the late stage. This is because solute transport from the surrounding liquid into pore plays a more significant role than pore volume expansion. An increase in bubble location enhances increasing rate of solute concentration at the cap. In view of solute concentration at the cap greater than initial solute concentration in liquid, solute transport is from the surrounding liquid to pore. An increase in bubble location enhances solute transfer across the cap. Solute gas pressure in the pore exhibits similar trend in solute concentration at cap, as shown in Fig. 5(c). An increase in bubble location increases solute gas pressure in the pore, whereas decreases apex radius of the cap. An increase in bubble location enhances decrease of contact angle in late stage, as shown in Fig. 5(d). The bubble growth rate-to-solidification rate ratio is negative and decreases its value during solidification. Decreasing rate of the bubble growth rate-to-solidification rate ratio increases with bubble location. Since the bubble growth rate-to-solidification rate ratio cannot approach zero, the cap cannot be entrapped [14, 15].

In Case 2b, an increase in dimensionless bubble location increases pore radius, as shown in Fig. 6(a). It is impossible to entrap the cap into solid. In contrast to Figs. 4(b) and 5(b), dimensionless solute concentration at the cap maintains constant in the early stage and then decreases rapidly in the late stage, as shown in Fig. 6(b). This is attributed to pore volume expansion. An increase in dimensionless bubble location increases solute concentration at the cap and its decreasing rate in the late stage. The corresponding dimensionless solute gas pressure in the pore and apex radius of the cap decreases

https://doi.org/10.1017/jmech.2017.90 Published online by Cambridge University Press

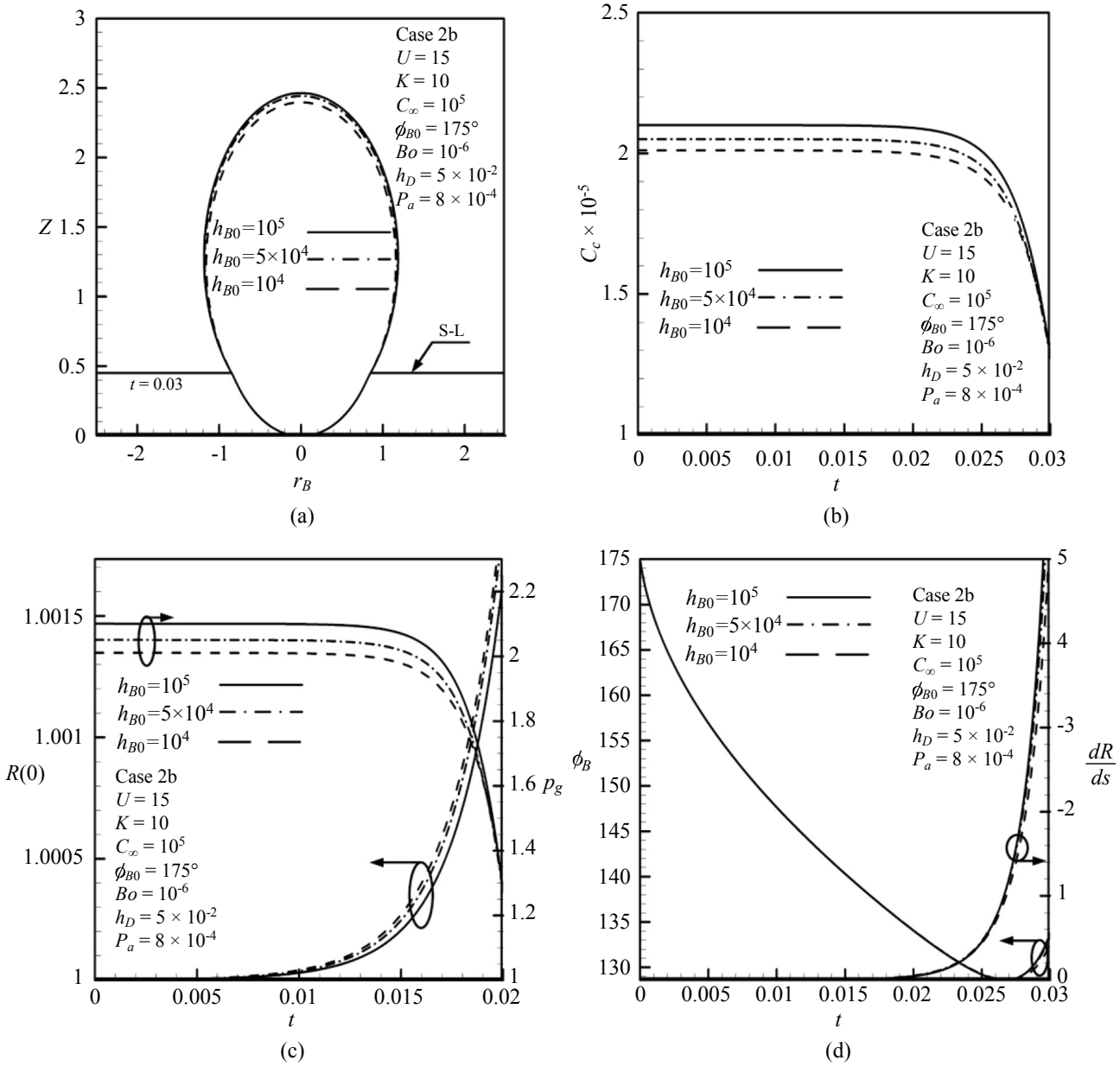


Fig. 6 Predicted (a) pore shape, and (b) dimensionless solute concentration at the cap, (c) dimensionless apex radius and solute gas pressure, and (d) contact angle and bubble growth rate-to-solidification rate ratio as functions of time for different dimensionless bubble locations in Case 2b.

and increases rapidly in the late stage, respectively, as shown in Fig. 6(c). Contact angle decreases and then increases rapidly during solidification for different bubble locations, as shown in Fig. 6(d). The time for occurrence of the minimum of contact angle decreases as bubble location increases. The positive bubble growth rate-to-solidification rate ratio increases rapidly in the late stage. The bubble cap therefore cannot be entrapped in solid.

4. CONCLUSIONS

Conclusions drawn are the following:

Case 1:

Solute is transport from the pore to surrounding liquid in the early stage. Pore radius and time for bubble entrapment increases with dimensionless bubble location. Solute concentration at the cap and solute gas pressure in the pore drops rapidly in early stage, whereas maintains relatively constant in late stage. They are attributed to additive and competitive effects between expansion of pore volume and solute transport across the cap, respectively. Since solute gas pressure in the pore decreases, apex radius increases with bubble location during solidification. An increase in bubble location increases and slightly decreases solute concentration at the cap and solute gas pressure in the pore in the early and late stages, respectively. This is attributed to increased solute gas pressure in the pore resulting in an increase in solute concentration at the cap in physico-chemical equilibrium.

https://doi.org/10.1017/jmech.2017.90 Published online by Cambridge University Press

An increase in bubble location enhances solute transport from the pore through cap to surrounding liquid in the early stage, and vice versa in the late stage. An increase in bubble location reduces drop of contact angle in early stage. Contact angle then maintains a relative constant value near 90 degrees for a long period, which increases with bubble location. Since increase in bubble location delays the bubble growth rate-to-solidification rate ratio to become zero at which contact angle passes through 90 degrees, leading to a delayed entrapment of the bubble.

Case 2:

Solute is transport from the surrounding liquid into submerged cap during solidification. Pore radius increases with bubble location. An isolate pore cannot be formed, because the bubble growth rate-to-solidification rate ratio cannot approach zero. An increase in bubble location increases solute concentration at the cap and solute gas pressure in the pore, and decreases apex radius and contact angle. In Case 2a: Solute concentration at the cap and solute gas pressure in the pore are primarily affected by solute transport from the surrounding liquid into pore. An increase in bubble location significantly enhances increasing rates of solute concentration at the cap and solute gas pressure in the pore, and decreasing rate of apex radius in the late stage. In Case 2b: Solute concentration at the cap and solute gas pressure in the pore are primarily affected by expansion rate of pore volume. An increase in bubble location significantly enhances decreasing rates of solute gas pressure in the pore and solute gas concentration at the cap in the late stage. Contact angle decreases and then increases rapidly during solidification. The time for occurrence of the minimum of contact angle decreases as bubble location increases.

ACKNOWLEDGEMENTS

This work is supported by NSC 102-2221-E-110-038, ROC

NOMENCLATURE

A_c cap surface area $\approx 2\pi R^2(0)(1-\cos\phi_B)$

Bo Bond number $\equiv \rho g\tilde{R}_0^2/\sigma$

C_∞ initial solute concentration $= \tilde{C}_\infty \tilde{R}_u \tilde{T}/\rho g\tilde{R}_0$

D solute diffusivity

h_B liquid depth, as illustrated in Fig. 1(a)

h_D mass transfer coefficient $= \tilde{h}_D \tilde{R}_0/\tilde{D}$

K Henry's law constant $= \tilde{K}/\tilde{R}_u\tilde{T}$

p pressure, $p \equiv \tilde{p}\tilde{R}_0/\sigma$

r cylindrical coordinate $\equiv \tilde{r}/\tilde{R}_0$

R radius $\equiv \tilde{R}/\tilde{R}_0$

$R(0)$ radius of curvature at micro-bubble apex

$\tilde{R}_u$ universal gas constant

s solidification front location

t time $\equiv \tilde{t}\tilde{D}/\tilde{R}_0^2$

U solidification rate = ds/dt

V volume $\equiv \tilde{V}/\tilde{R}_0^3$

z cylindrical coordinate, $\equiv \tilde{z}/\tilde{R}_0$

Greek letter

ϕ inclination angle

Subscripts

a atmosphere

B base

g gas

0 initial state

Superscripts

~ dimensional quantity

REFERENCES

1. Nakajima, H., "Fabrication, Properties and Application of Porous Metals with Directional Pores," *Progress in Materials Science*, **52**, pp. 1091-1173 (2007).
2. Yoshimura, K., Inada, T. and Koyama, S.,"Growth of Spherical and Cylindrical Oxygen Bubbles at an Ice-Water Interface," *Crystal Growth and Design*, **8**, pp. 2108-2115 (2008).
3. Kou, S., *Welding Metallurgy*, Wiley, New York (1987).
4. Sulfredge, C. D., Chow, L. C. and Tagavi, K. A., "Artificial Dispersal of Void Patterns in Unidirectional Freezing," *Experimental Heat Transfer,* **6**, pp. 389-409 (1993).
5. Zhao, H., White, D. R. and DebRoy, T., "Current Issues and Problems in Laser Welding of Automotive Aluminum Alloys," *International Materials Reviews,* **44**, pp. 238-266 (1999).
6. Elmer, J. W., Vaja, J., Carlton, H. D. and Pong, R., "The Effect of Ar and N2 Shielding Gas on Laser Weld Porosity in Steel, Stainless Steels, and Nickel," *Welding Journal*, **94**, pp. 313-325 (2015).
7. Wei, P. S., Huang, C. C. and Lee, K. W., "Nucleation of Bubbles on a Solidification Front-Experiment and Analysis," *Metallurgical and Materials Transactions B*, **34**, pp. 321-332 (2003).
8. Catalina, A. V., Stefanescu, D. M., Sen, S. and Kaukler, W. F., "Interactions of Porosity with a Planar Solid/Liquid Interface," *Metallurgical and Materials Transactions A*, **35**, pp. 1525-1538 (2004).
9. Tatarchenko, V. A., "Cylindrical Pores in a Growing Crystal," *Journal of Crystal Growth*, **143**, pp.

https://doi.org/10.1017/jmech.2017.90 Published online by Cambridge University Press

294-300 (1994).

10. Wei, P. S. and Ho, C. Y., "An Analytical Self-Consistent Determination of a Bubble with a Deformed Cap Trapped in Solid during Solidification," *Metallurgical and Materials Transactions B*, **33**, pp. 91-100 (2002).
11. Wei, P. S., "Thermal Science of Weld Bead Defects: A Review," in Special Issue on Advanced Thermal Processing, *Journal of Heat Transfer,* **133**, 031005 (2011).
12. Park, J. S., Hyun, S. K., Suzuki, S. and Nakajima, H., "Effect of Transference Velocity and Hydrogen Pressure on Porosity and Pore Morphology of Lotus-Type Porous Copper Fabricated by a Continuous Casting Technique," *Acta Materialia*, **55**, pp. 5646-5654 (2007).
13. Drenchev, L., Sobczak, J., Sobczak, N., Sha, W. and Malinov, S., "A Comprehensive Model of Ordered Porosity Formation," *Acta Materialia*, **55**, pp. 6459-6471 (2007).
14. Wei, P. S. and Hsiao, S. Y., "Pore Shape Development from a Bubble Captured by a Solidification Front," *International Journal of Heat and Mass Transfer,* **55**, pp. 8129-8138 (2012).
15. Wei, P. S. and Hsiao, S. Y., "Pore Formation from Bubble Entrapment by a Solidification Front," *American Journal of Heat and Mass Transfer,* **2**, pp. 76-88 (2015).
16. Jones, S. F., Evans, G. M. and Galvin, K. P., "The Cycle of Bubble Production from a Gas Cavity in a Supersaturated Solution," *Advances in Colloid and Interface Science*, **80**, pp. 51-84 (1999).
17. Cox, M. C., Anilkumar, A. V., Grugel, R. N. and Lee, C. P., "Effect of Step-Wise Change in Processing Pressure on Isolated Pore Growth during Controlled Directional Solidification in Small Channels," *Journal of Crystal Growth,* **311**, pp. 327-336 (2009).
18. Lee, C. P., Anilkumar, A. V., Cox, M. C., Lioi, C. B. and Grugel, R. N., "Evolution of Elongated Pores at the Melt-Solid Interface during Controlled Directional Solidification," *Acta Materialia*, **61**, pp. 3752-3757 (2013).
19. Wei, P. S. and Hsiao, C. C., "Microbubble or Pendant Drop Control Described by a General Phase Diagram," *International Journal of Heat and Mass Transfer,* **52**, pp. 1304-1312 (2009).
20. Wei, P. S., Huang, C. C., Wang, Z. P., Chen, K. Y. and Lin, C. H., "Growths of Bubble/Pore Sizes in Solid during Solidification -An In Situ Measurement and Analysis," *Journal of Crystal Growth*, **270**, pp. 662-673 (2004).

(Manuscript received July 6, 2017,
accepted for publication August 17, 2017.)

https://doi.org/10.1017/jmech.2017.90 Published online by Cambridge University Press